PCCP

RSC Publishing

PAPER

View Article Online
View Journal | View Issue

Synthesis of Mn-doped α-$Ni(OH)_2$ nanosheets assisted by liquid-phase laser ablation and their electrochemical properties

Cite this: *Phys. Chem. Chem. Phys.*, 2013, **15**, 5684

Hemin Zhang, Jun Liu, Yixing Ye, Zhenfei Tian and Changhao Liang*

Received 19th January 2013,
Accepted 20th February 2013

DOI: 10.1039/c3cp50248a

www.rsc.org/pccp

We designed a new strategy, namely, the laser ablation of a target material in an aqueous ionic solution, to prepare Mn-doped $Ni(OH)_2$ nanosheets based on reactions between the pulsed laser-induced plasma plume of Mn and the surrounding $NiCl_2$ solution. The crystalline phase, morphology and structure of the as-derived products are characterised by X-ray diffraction, field-emission scanning electron microscopy, transmission electron microscopy and X-ray photoelectron spectroscopy. Results indicate the hierarchical assembly of numerous tiny nanosheet building blocks into a Mn-doped α-$Ni(OH)_2$ spherical structure. Importantly, the positive electrode made of Mn-doped α-$Ni(OH)_2$ nanosheets exhibits a high specific capacitance of ~1000 F g^{-1} under a current density of 5 A g^{-1}, concurrently possessing excellent cycling ability. This novel strategy may offer researchers an alternative for designing interesting solid targets and ionic solutions towards the fabrication of other new nanostructures for fundamental research and potential applications.

1. Introduction

Considering the depletion of fossil fuels and the deterioration of environmental pollution, renewable and clean energy sources, as well as advanced energy storage and management devices, have become increasingly important in the 21st century.[1] Supercapacitors, known as potential electrochemical supercapacitors or ultracapacitors, are attracting considerable interest because of their promising characteristics for energy storage as a result of their fast energy delivery, high-power performance and long life-cycling behaviour.[2,3] In recent years, $Ni(OH)_2$ has received much attention because of its high capacitance, well-defined electrochemical performance and low cost.[4,5] In particular, given its metastable phase, α-$Ni(OH)_2$ can easily be manipulated in terms of morphology, basal spacing and type of inorganic material. These characteristics make α-$Ni(OH)_2$ a promising material for electrochemical capacitors and secondary batteries. As a positive electrode, α-$Ni(OH)_2$ exhibits a good performance in highly reversible energy storage, long-term cycling stability and charge–discharge kinetics in rechargeable alkaline nickel–metal hydride (Ni–MH) batteries.[6,7] However, these Ni–MH batteries operate in a high-temperature environment of over 40 °C where many cells are connected in series to provide a high system voltage. Under this condition, oxygen evolution easily occurs and leads to a significant decline in the charge efficiency. The addition of metal oxides to electrodes[8] can increase the potential of oxygen evolution and suppress γ-NiOOH formation during the charge–discharge cycling. For example, the addition of cobalt oxide can further improve the high electronic and proton conductivity, and result in a much higher performance in terms of both discharge capacity and cycle life.[9] Unfortunately, cobalt is expensive and toxic. In the search for ideal alternatives,[10] the addition of manganese oxide and/or doping with manganese element is considered to be particularly attractive for improving performance at elevated temperatures because of its low cost, nontoxicity and high average potential.

Charge–discharge reactions are much more complex in nickel hydroxide electrodes, involving four phases [α-$Ni(OH)_2$, β-$Ni(OH)_2$, β-NiOOH and γ-NiOOH] during the lifetime of an electrode.[11] The formation of these phases is accompanied with volume expansion or swelling of the nickel hydroxide electrode, leading to poor effective contact between particles of active materials, thereby increasing the resistance of the electrode reaction especially at high-temperature or high-rate charge–discharge.[12] The electrochemical performance of $Ni(OH)_2$ is significantly affected by its crystal structure, size and morphology. The size in nanoscale dimension can largely enhance the specific surface area, fast redox reaction and short diffusion

Key Laboratory of Materials Physics and Anhui Key Laboratory of Nanomaterials and Nanotechnology, Institute of Solid State Physics, Hefei Institutes of Physical Science, Chinese Academy of Sciences, Hefei, 230031, P. R. China.
E-mail: chliang@issp.ac.cn; Fax: +86-551-65591434; Tel: +86-551-65591129

path in the solid phase, resulting in improved electrochemical properties.[13–15] The morphology of $Ni(OH)_2$ also considerably influences its electrochemical properties.[16–18] Numerous studies have focused on the development of robust composite nanostructures with rich hierarchical (meso- and macro-) porosity and large specific surface areas. These features inevitably lead to the ability of electrolyte ions to make more efficient contact with more electroactive sites for Faradic energy storage, even at high current densities.[19,20] Therefore, electrode materials that self-assemble with nano/micro hierarchical superstructures are considered as some of the best systems, with the advantages of nanometer-sized building blocks and micro- or submicrometer-sized assemblies. These assemblies, which possess desirable mechanical properties and good stability,[21] can suppress the development of an inner-pore volume, increasing the density of the active material itself. Particularly, nanoscale building blocks can effectively shorten the diffusion times and achieve favourable kinetics and high capacities.[18] The design and tailoring of hierarchical $Ni(OH)_2$ electroactive materials are of academic and practical importance. Various morphologies of $Ni(OH)_2$ such as nanowire, nanotube, nanosheet, mesoporous structure and hollow sphere have been synthesised through different chemical routes.[16,22–24]

Recently, laser ablation in liquid (LAL), a simple and green technique, has shown outstanding ability in fabricating a large variety of high-activity nanomaterials,[25–27] including core–shell nanostructures,[28,29] hollow nanoparticles,[30,31] quantum dots[32,33] and nanoparticles (or species),[34,35] as well as the extended technique of pulsed laser irradiation in liquid.[36–38] Importantly, the generated colloids that serve as distinctive precursors are able to produce novel structures.[39–41] To date, few attempts have been made to prepare doping nanostructures using this technique.[42,43] Given that the distinguishing structure feature of α-$Ni(OH)_2$ is its metastable phase, α-$Ni(OH)_2$ is difficult to synthesise because it can easily transform into the β-form, which has inferior electrochemical properties. Accordingly, this study aimed to synthesise hierarchical Mn-doped α-$Ni(OH)_2$ assemblies with potential application in super-capacitor positive electrodes.

2. Experimental details

2.1 Preparation of Mn-doped $Ni(OH)_2$ nanostructure

The nanostructure of Mn-doped α-$Ni(OH)_2$ was firstly synthesised using a pulsed LAL (PLAL) system. In a typical procedure, a manganese metal plate (99.99% purity) was first fixed on a supporter in a vessel filled with 12 mL of 0.01 M $NiCl_2$ solution. Upon irradiation of the metal plate, the vessel was rotated (10 rpm) by a motorised tunable stage. The metal plate was irradiated using a Nd:YAG pulsed laser at 1064 nm wavelength with energy density of 160 mJ per pulse, pulse duration of 10 ns and spot diameter of approximately 1.0 mm (Scheme 1). The liquid height was set to 1.2 mm from the target surface. After irradiation, the suspension was separately placed in four tubes and centrifuged at 8000 rpm for 8 min.

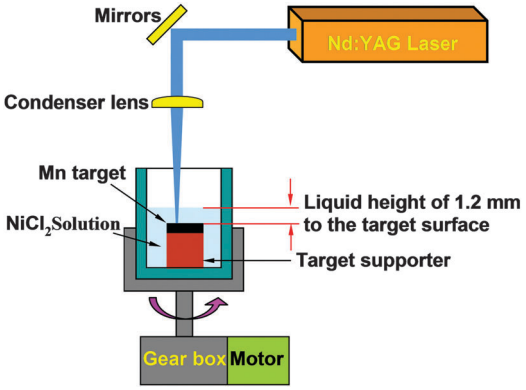

Scheme 1 Schematic of the synthesis of Mn-doped α-$Ni(OH)_2$ nanostructures.

The upper solutions (containing some manganese oxide nanoparticles) were removed from the tubes. Ethanol and deionised water were added, and then ultrasonic dispersion was performed for 8 min. This procedure was repeated five times to obtain pure $Ni(OH)_2$ nanosheets without any attached manganese oxide nanoparticles. The ablation time was 5 min for each experiment, and the experiment was repeated to obtain sufficient powder products for analyses. The obtained powder products were kept in a vacuum dry box at 30 °C.

2.2 Characterisation of Mn-doped α-$Ni(OH)_2$ nanostructure

The collected powder products were prepared as specimens on glass substrates and analysed using an X-ray diffraction (XRD) system (Philips X'Pert) with CuKα radiation (λ = 0.15419 nm, scan step size = 0.033492° and time per step = 200.025 s). The morphology of the products was investigated using a field-emission scanning electron microscopy (FESEM) system (Sirion 200 FEG). Microstructure examination was performed using a transmission electron microscopy (TEM) system (JEOL, JEM-2010; 200 kV acceleration voltage) equipped with an Oxford INCA energy dispersive spectrometer. The TEM specimens were prepared by dispersing the powders in ethanol to form suspensions, and then dropping onto a carbon-coated Cu grid. X-ray photo-electron spectroscopy (XPS) analysis was performed with an AlKα X-ray source on a Thermo-VGESCALAB MKII spectrometer. For electrochemical measurements, 1 mg of the synthesised products was dispersed in ethanol with 1% PTFE binder. The suspension was drop dried into a 1 cm × 1 cm Ni foam (2 mm thick) for 1 h at 80 °C. The foam with the sample loaded was compressed at 20 MPa and held for 3 min prior to measurement. Cyclic voltammetry (CV) and galvanostatic charge–discharge measurements were carried out on an IM6ex (Zahner, Germany).

3. Results and discussions

3.1 XRD analysis

Fig. 1 shows the XRD pattern of the as-prepared Mn-doped α-$Ni(OH)_2$. The diffraction peaks at 2θ values of 11.4°, 22.8°, 33.4°, 34.4°, 45.9°, 59.9° and 61.2° are assigned to the (003),

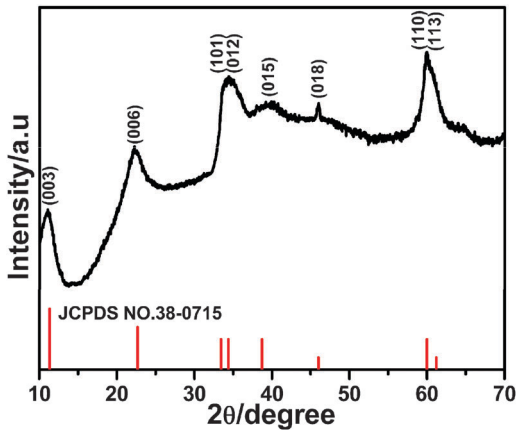

Fig. 1 XRD spectra of Mn-doped $Ni(OH)_2$.

(006), (101), (012), (015), (018), (110) and (113) diffractions, respectively, of hexagonal α-$Ni(OH)_2 \cdot 0.75H_2O$ with the lattice parameters a = 3.08 Å and c = 23.41 Å (JCPDS NO. 38-0715). No other diffraction peak is found, demonstrating that the prepared product is pure. In addition, the (003), (006), (101), (012) and (110) diffraction peaks are obviously broader, indicating the nanoscale size of the product. Importantly, as shown in Table 1, the 2θ values of the three strong diffraction peaks of the sample display a red shift in different degrees, and the corresponding d values accordingly decrease. This result suggests a lattice distortion of the metastable α-$Ni(OH)_2$. In addition, the lattice planes of (003) and (006) present high diffraction intensity and large half-width, which may be due to the preferential orientation growth and relatively small dimensional size of crystalline planes (00h). No Mn-related phases are detected by XRD analysis, indicating that the lattice distortion of α-$Ni(OH)_2$ may be induced by the doped Mn.

3.2 Morphology and structure of Mn-doped α-$Ni(OH)_2$

The FESEM images of the as-synthesised Mn-doped α-$Ni(OH)_2$ structure are presented in Fig. 2. Two typical morphologies can be observed (Fig. 2a and b), the majority displaying aggregated nanosheets in irregular shape and a few showing spherical assemblies of nanosheets (the marks in Fig. 2a). The corresponding TEM images of the typical structure are shown in Fig. 3, further demonstrating that the spherical structures are assemblies of many tiny nanosheets (Fig. 3a). Intriguingly, the dispersed nanosheets also display beautiful flower-like shapes. A single nanosheet is ultrathin even if curled; its thickness is only approximately 3 nm (Fig. 3d). When the ultrathin nanosheets are under high-energy electron beam irradiation,

Table 1 Change in 2θ (°) and the corresponding d (Å) values for the three strong peaks

Lattice planes	2θ (°)	d (Å)	2$\theta_{0.01}$ (°)	$d_{0.01}$ (Å)
(003)	11.4	7.8	11.5	7.7
(006)	22.7	3.9	22.8	3.8
(110)	60.0	1.5	59.8	1.5

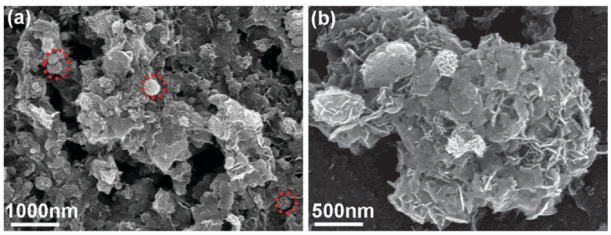

Fig. 2 FESEM images of Mn-doped $Ni(OH)_2$.

they are unstable and some of them easily change into NiO. For example, under HRTEM investigation, these nanosheets are dehydrated and transformed into the NiO phase, with the corresponding morphology displaying many holes (Fig. 3b). The HRTEM image (Fig. 3c) demonstrates that the marked lattice spacing of 0.21 nm is concordant with the (200) d-spacing of NiO. The phase transformation is also further confirmed by two sets of corresponding selected-area electron diffraction (SAED) patterns (Fig. 3e). Energy dispersive spectrometry (EDS) analysis of the aggregated nanosheets (Fig. 3f) demonstrates the uniform distribution of Mn, Ni and O elements, as shown in Fig. 3g–i, and also provides the Mn content in the sample, which is ~17.1 wt%.

EDS measurements confirm the existence of Mn element in the $Ni(OH)_2$ nanosheets. To reveal the valence states of Mn within $Ni(OH)_2$, the XPS spectra of the Mn-doped α-$Ni(OH)_2$ are further measured. The relative peak shifts from the electrostatic charge-up are calibrated using the C1s peak at 284.6 eV. The full XPS spectrum of the Mn-doped α-$Ni(OH)_2$ is shown in Fig. 4a. Mn, Ni, O and C elements are shown with sharp photoelectron peaks at binding energies of 50 eV (Mn3p), 68 eV (Ni3p), 285 eV (C1s), 531 eV (O1s), 642 eV (Mn2p) and 855 eV (Ni2p). The characteristic peak with a binding energy of 855.5 eV is assigned to $Ni2p_{3/2}$ in $Ni(OH)_2$, as shown in Fig. 4b. The XPS spectrum confined to the Mn2p window (Fig. 4c) shows the binding energy of the $Mn2p_{1/2}$ and $Mn2p_{3/2}$ peaks corresponding to 654.1 and 642.4 eV, respectively. In addition, the energy separation between the $2p_{3/2}$ and $2p_{1/2}$ states is 11.7 eV. These results agree well with the reported data of $Mn2p_{1/2}$ and $Mn2p_{3/2}$ in MnO_2,[44,45] indicating that the Mn atoms doped in the $Ni(OH)_2$ lattices mainly exist in the form of Mn(IV) ions, differing from the Mn atoms in the lattices of Mn_3O_4 nanocrystals that can be generated by PLAL as in our previous report.[35] The quantitative XPS analysis of Mn^{IV}-doped α-$Ni(OH)_2 \cdot 0.75H_2O$ shows that the atomic ratio of Mn to Ni is ~1 : 3.2. From this ratio, the Mn content of ~15.9 wt% in the sample is calculated, and this value is close to the EDS result above. The composition of metal (Fe, Co, Zn and so on)/nickel hydrous oxides with this ratio is very helpful in lowering the oxygen evolution by catalysing the reaction.[46] The as-synthesised Mn-doped α-$Ni(OH)_2$ is expected to have outstanding applications in alkaline rechargeable batteries and electrocatalytic electrolysis for hydrogen production.

3.3 Formation mechanism of the Mn-doped α-$Ni(OH)_2$

A possible formation mechanism is proposed in Scheme 2. When the high-energy pulsed laser is irradiated on the Mn

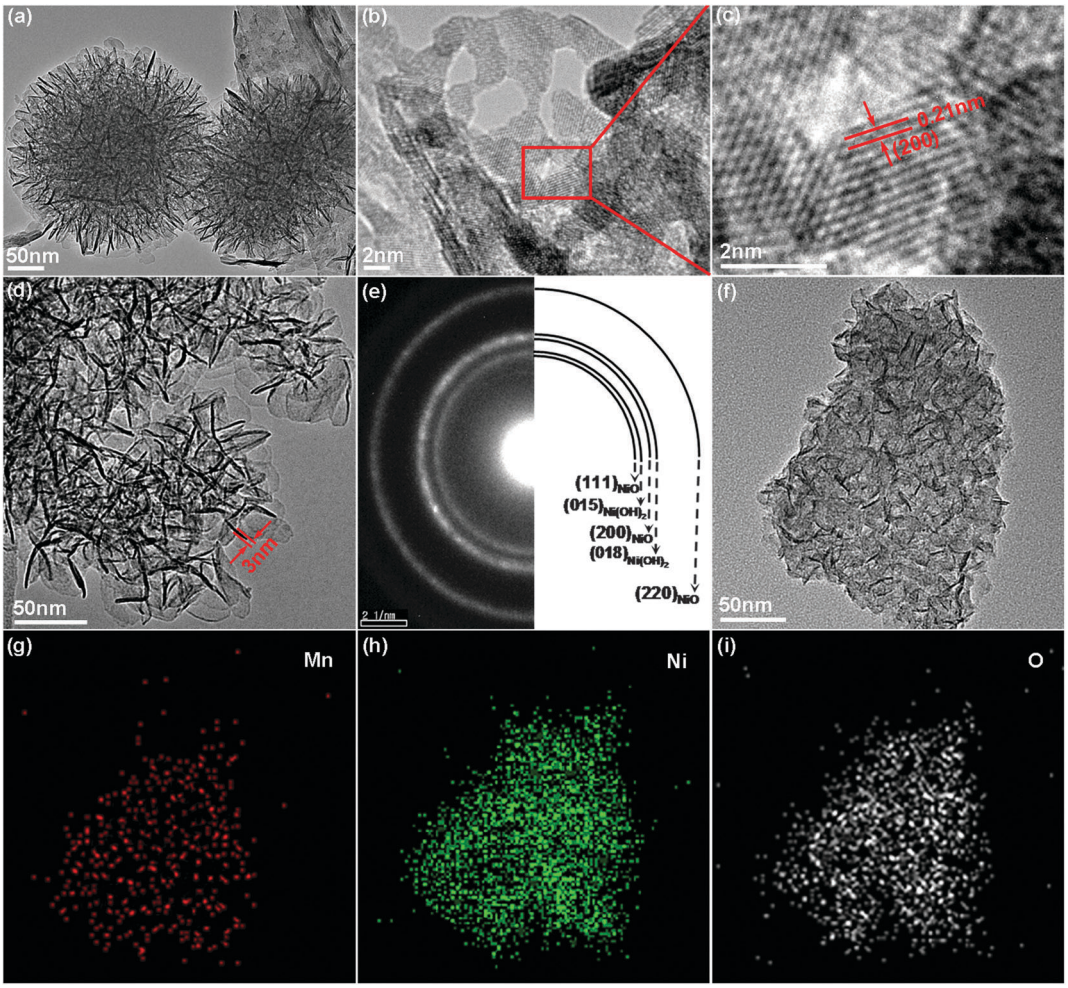

Fig. 3 (a), (b), (d), and (f) TEM and (c) HRTEM images, (e) the corresponding SAED pattern and (g)–(i) EDS mapping of the Mn-doped $Ni(OH)_2$ nanosheets obtained by LAL of Mn target in $NiCl_2$ solution.

target in the 0.01 M $NiCl_2$ aqueous solution, a plasma plume is generated on the surface of the Mn target, containing electrons, manganese atoms, various manganese ions and their clusters. Subsequently, the plasma plume possessing high temperature and high pressure expands at ultrasonic speed and vigorously reacts with the surrounding aqueous solution. The processes involved in such reaction may generate many hydrogen radicals, hydroxyl groups, hydrogen and hydroxide ions. Our previous study has demonstrated that many hydroxyl ions are produced in the formation of Mn_3O_4 based on the change in pH.[35] In the current study, most hydroxyl ions generated combine with the surrounding Ni^{2+} and form the nuclei of α-$Ni(OH)_2$ in the rapid expansion of the plasma plume. Active species such as manganese atoms and ions from the plasma plume may substitute Ni ions or intercalate into layers of α-$Ni(OH)_2$ nanosheets during the growth of the $Ni(OH)_2$ nuclei. Simultaneously, H_2O molecules, Cl^{-1} ions and even the initially formed Mn_3O_4 clusters (<3.2 nm) easily penetrate the intercalated layers of $Ni(OH)_2$ because of its interlayer spacing variation within the range of 0.75 nm to 3.2 nm.[47] In general, the colloidal nanoparticles produced by LAL in aqueous solution possess the features of metastable structure,[40] high-density surface defects[35] and high reaction activities,[41,43] readily resulting in nanostructures of self-assemblies. In the case of our experiment, the initially formed $Ni(OH)_2$ nanosheets with metastable phase and clean surfaces tend to construct flower-like nanostructures (top right corner of Scheme 2). On the other hand, the induced cavity bubbles generated in the evolution of the plasma plume provide opportunities for forming $Ni(OH)_2$ nuclei, which finally grow into spherical assemblies in hierarchical structure (lower right corner of Scheme 2).

3.4 Electrochemical properties of Mn-doped α-$Ni(OH)_2$ electrode

The electrochemical properties and specific capacitance of Mn-doped α-$Ni(OH)_2$ are investigated by CV and galvanostatic charge–discharge measurements in a three-electrode system. The products are coated onto nickel foam as the working electrode. The reference electrode and counter electrode are Ag/AgCl and platinum, respectively. All experiments are conducted in 6 M KOH as the electrolyte at ambient temperature. A recent report demonstrated that the background signal

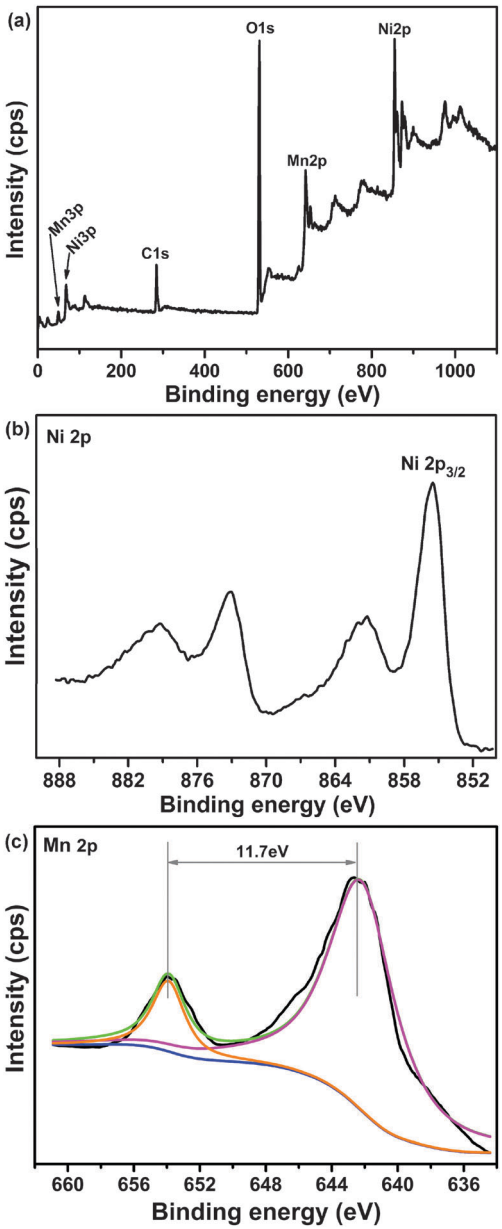

Fig. 4 (a) Full XPS spectrum of Mn-doped $Ni(OH)_2$, and high-resolution spectra of (b) Ni2p and (c) Mn2p.

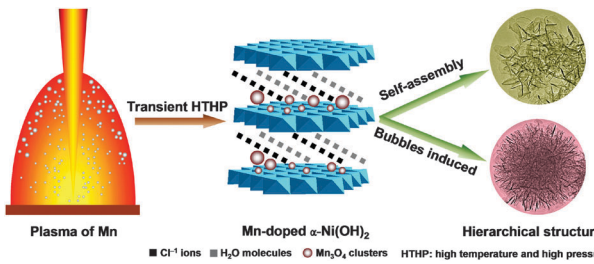

Scheme 2 Formation process of Mn-doped α-$Ni(OH)_2$ hierarchical structures.

of blank Ni foam is negligible in 6 M KOH.[48] The typical CV curve of Mn-doped α-$Ni(OH)_2$ is shown in Fig. 5a. The curve has

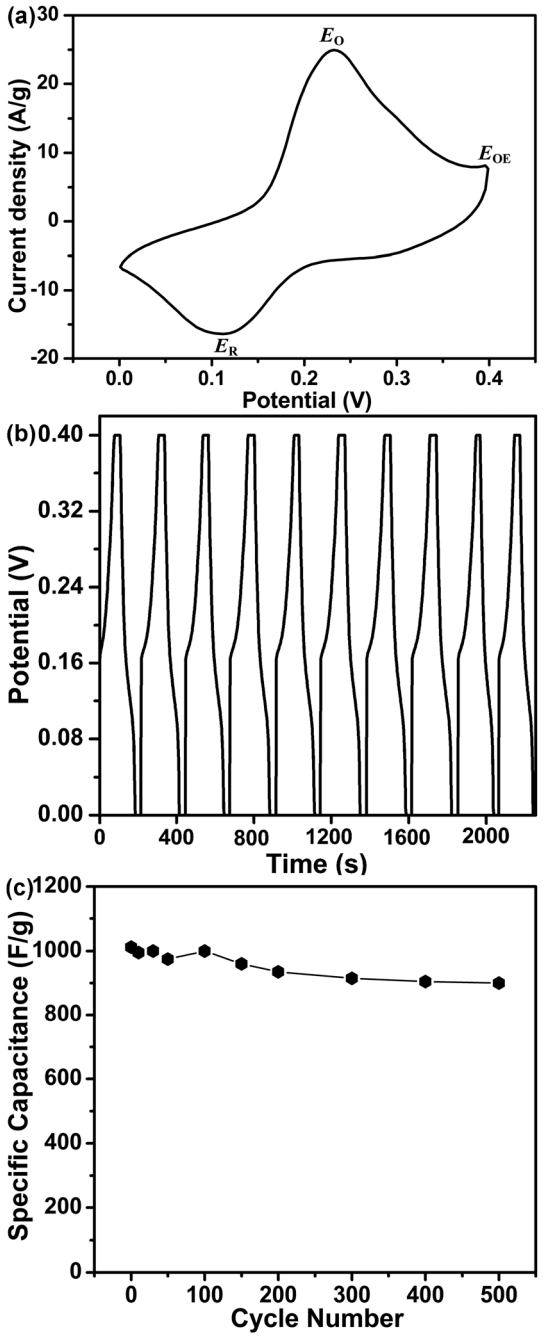

Fig. 5 (a) Cyclic voltammograms (scan rate: 10 mV s^{-1}) of the supercapacitor built from the Mn-doped $Ni(OH)_2$ nanostructure. (b) Galvanostatic charge–discharge curves at a charging rate of 5 A g^{-1}. (c) Cycle performance at 4 mA cm^{-2} in 6 M KOH solution.

two intense peaks. One peak (E_O) is anodic (positive current density) during the oxidation reaction of Ni^{2+} to Ni^{3+}, and the other (E_R) is cathodic (negative current density) during the reverse process. These peaks result from the fast and reversible redox processes that occur at the interface of Mn-doped α-$Ni(OH)_2$ and KOH electrolyte. The reactions can be described by eqn (1):

$$\alpha\text{-}Ni(OH)_2 + OH^- \leftrightarrow \gamma\text{-}NiOOH + H_2O + e^- \quad (1)$$

The galvanostatic charge–discharge curves of the Mn-doped α-$Ni(OH)_2$ electrode in 6 M KOH solution are shown in Fig. 5b. The regular shape of the curves indicates that the system undergoes a reversible charge–discharge process and has good supercapacitor stability. The value of the specific capacitance of the electrode can be calculated according to eqn (2):

$$C_{SP} = \frac{it}{m\Delta v} \quad (2)$$

where i, t, m and Δv are the constant current (A), discharge time (s), mass of the active materials (g) and total potential deviation (V), respectively. The specific capacitance of the Mn-doped α-$Ni(OH)_2$ electrode is approximately 1000 F g^{-1}, which is calculated from the galvanostatic charge–discharge curves (Fig. 5b) under a current density of 5 A g^{-1}. The value of its specific capacitance is much higher than the values obtained with a graphene nanosheet–Ni^{2+}–Al^{3+} composite[1] and with α-$Ni(OH)_2$ intercalated with anions.[49] The endurance test of the sample is conducted by galvanostatic charging/discharging between 0 and 0.4 V at a nominal 4 mA cm^{-2} rate for 500 cycles. The specific capacitance as a function of cycle number is plotted in Fig. 5c, indicating that the degradation of the specific capacitance is approximately 9% after 500 cycles. These data demonstrated that the preparation of Mn-doped α-$Ni(OH)_2$ using this unique strategy has a significant potential application in advanced supercapacitors.

4. Conclusions

A unique strategy without any hard/soft template is developed to obtain hierarchical Mn-doped α-$Ni(OH)_2$ nanostructures by laser ablation of a Mn target in $NiCl_2$ aqueous solution. The experimental results demonstrate that the generated Mn-doped α-$Ni(OH)_2$ hierarchical structures are assembled from a large number of nanosheets, which may be beneficial to a high specific capacitance of ~1000 F g^{-1} at a charge and discharge current density of 5 A g^{-1} and good cycling ability. The successful construction of the Mn-doped α-$Ni(OH)_2$ structure also extends the scope of nanostructures that LAL can synthesise, and expands the applications of the LAL technique.

Acknowledgements

This work was financially supported by the National Natural Science Foundation of China (grant no. 11204308, 11174287, 10974204, 50931002), Hundred Talent Program of Chinese Academy of Sciences.

Notes and references

1 Z. Gao, J. Wang, Z. Li, W. Yang, B. Wang, M. Hou, Y. He, Q. Liu, T. Mann, P. Yang, M. Zhang and L. Liu, *Chem. Mater.*, 2011, **23**, 3509–3516.
2 Z. Y. Lu, Z. Chang, W. Zhu and X. M. Sun, *Chem. Commun.*, 2011, **47**, 9651–9653.
3 Y. Zhu, S. Murali, M. D. Stoller, K. J. Ganesh, W. Cai, P. J. Ferreira, A. Pirkle, R. M. Wallace, K. A. Cychosz, M. Thommes, D. Su, E. A. Stach and R. S. Ruoff, *Science*, 2011, **332**, 1537–1541.
4 H. L. Wang, H. S. Casalongue, Y. Y. Liang and H. J. Dai, *J. Am. Chem. Soc.*, 2010, **132**, 7472–7477.
5 G. X. Hu, C. X. Li and H. Gong, *J. Power Sources*, 2010, **195**, 6977–6981.
6 C. Y. Wang, S. Zhong, D. H. Bradhurst, H. K. Liu and S. X. Dou, *J. Alloys Compd.*, 2002, **330–332**, 802–805.
7 W. K. Hu and D. Noréus, *Chem. Mater.*, 2003, **15**, 974–978.
8 X. Mi, X. P. Gao, C. Y. Jiang, M. M. Geng, J. Yan and C. R. Wan, *Electrochim. Acta*, 2004, **49**, 3361–3366.
9 A. B. Yuan, S. A. Cheng, J. Q. Zhang and C. A. Cao, *J. Power Sources*, 1999, **77**, 178–182.
10 R. Koksbang, J. Barker, H. Shi and M. Y. Saïdi, *Solid State Ionics*, 1996, **84**, 1–21.
11 H. Bode, K. Dehmelt and J. Witte, *Electrochim. Acta*, 1966, **11**, 1079–1087.
12 D. Singh, *J. Electrochem. Soc.*, 1998, **145**, 116–120.
13 D. E. Reisner, A. J. Salkind, P. R. Strutt and T. D. Xiao, *J. Power Sources*, 1997, **65**, 231–233.
14 X. H. Liu and L. Yu, *J. Power Sources*, 2004, **128**, 326–330.
15 X. J. Han, X. M. Xie, C. Q. Xu, D. R. Zhou and Y. L. Ma, *Opt. Mater.*, 2003, **23**, 465–470.
16 D. N. Yang, R. M. Wang, M. S. He, J. Zhang and Z. F. Liu, *J. Phys. Chem. B*, 2005, **109**, 7654–7658.
17 G. R. Fu, Z. A. Hu, L. J. Xie, X. Q. Jin, Y. L. Xie, Y. X. Wang, Z. Y. Zhang, Y. Y. Yang and H. Y. Wu, *Int. J. Electrochem. Sci.*, 2009, **4**, 1052–1062.
18 C. Z. Yuan, X. G. Zhang, L. H. Su, B. Gao and L. F. Shen, *J. Mater. Chem.*, 2009, **19**, 5772–5777.
19 F. Jiao, A. H. Hill, A. Harrison, A. Berko, A. V. Chadwick and P. G. Bruce, *J. Am. Chem. Soc.*, 2008, **130**, 5262–5266.
20 D. W. Wang, F. Li, M. Liu, G. Q. Lu and H. M. Cheng, *Angew. Chem., Int. Ed.*, 2008, **47**, 373–376.
21 J. S. Hu, L. S. Zhong, W. G. Song and L. J. Wan, *Adv. Mater.*, 2008, **20**, 2977–2982.
22 B. J. Li, M. Ai and Z. Xu, *Chem. Commun.*, 2010, **46**, 6267–6269.
23 G. Duan, W. Cai, Y. Luo and F. Sun, *Adv. Funct. Mater.*, 2007, **17**, 644–650.
24 F. S. Cai, G. Y. Zhang, J. Chen, X. L. Gou, H. K. Liu and S. X. Dou, *Angew. Chem., Int. Ed.*, 2004, **43**, 4212–4216.
25 S. Barcikowski and F. Mafune, *J. Phys. Chem. C*, 2011, **115**, 4985.
26 F. Mafuné, J.-Y. Kohno, Y. Takeda and T. Kondow, *J. Am. Chem. Soc.*, 2003, **125**, 1686–1687.
27 V. Amendola, P. Riello, S. Polizzi, S. Fiameni, C. Innocenti, C. Sangregorio and M. Meneghetti, *J. Mater. Chem.*, 2011, **21**, 18665–18673.
28 K. Y. Niu, J. Yang, S. A. Kulinich, J. Sun, H. Li and X. W. Du, *J. Am. Chem. Soc.*, 2010, **132**, 9184–9189.
29 Q. Li, C. H. Liang, Z. F. Tian, J. Zhang, H. M. Zhang and W. P. Cai, *CrystEngComm*, 2012, **14**, 3236–3240.
30 Z. J. Yan, R. Q. Bao, C. M. Busta and D. B. Chrisey, *Nanotechnology*, 2011, **22**, 265610.
31 K. Y. Niu, J. Yang, J. Sun and X. W. Du, *Nanotechnology*, 2010, **21**, 295604.

32 S. C. Singh, S. K. Mishra, R. K. Srivastava and R. Gopal, *J. Phys. Chem. C*, 2010, **114**, 17374–17384.
33 S. K. Yang, W. P. Cai, H. B. Zeng and X. X. Xu, *J. Mater. Chem.*, 2009, **19**, 7119–7123.
34 Z. F. Tian, C. H. Liang, J. Liu, H. M. Zhang and L. D. Zhang, *J. Mater. Chem.*, 2011, **21**, 18242–18247.
35 H. M. Zhang, C. H. Liang, Z. F. Tian, G. Z. Wang and W. P. Cai, *J. Phys. Chem. C*, 2010, **114**, 12524–12528.
36 H. Wang, M. Miyauchi, Y. Ishikawa, A. Pyatenko, N. Koshizaki, Y. Li, L. Li, X. Li, Y. Bando and D. Golberg, *J. Am. Chem. Soc.*, 2011, **133**, 19102–19109.
37 H. Q. Wang, A. Pyatenko, K. Kawaguchi, X. Y. Li, Z. Swiatkowska-Warkocka and N. Koshizaki, *Angew. Chem., Int. Ed.*, 2010, **49**, 6361–6364.
38 H. Q. Wang, N. Koshizaki, L. Li, L. C. Jia, K. Kawaguchi, X. Y. Li, A. Pyatenko, Z. Swiatkowska-Warkocka, Y. Bando and D. Golberg, *Adv. Mater.*, 2011, **23**, 1865–1870.
39 H. M. Zhang, C. H. Liang, Z. F. Tian, G. Z. Wang and W. P. Cai, *CrystEngComm*, 2011, **13**, 1063–1066.
40 H. M. Zhang, C. H. Liang, Z. F. Tian, J. Liu and W. P. Cai, *CrystEngComm*, 2011, **13**, 4676–4682.
41 H. M. Zhang, C. H. Liang, J. Liu, Z. F. Tian, G. Z. Wang and W. P. Cai, *Langmuir*, 2012, **28**, 3938–3944.
42 J. Liu, C. H. Liang, H. M. Zhang, Z. F. Tian and S. Y. Zhang, *J. Phys. Chem. C*, 2012, **116**, 4986–4992.
43 J. Liu, C. H. Liang, H. M. Zhang, S. Y. Zhang and Z. F. Tian, *Chem. Commun.*, 2011, **47**, 8040–8042.
44 A. L. M. Reddy, M. M. Shaijumon, S. R. Gowda and P. M. Ajayan, *Nano Lett.*, 2009, **9**, 1002–1006.
45 J. F. Moulder, W. F. Stickle, P. E. Sobol and K. D. Bomben, *Physical Electronics Division*, Perkin-Elmer Corp., Eden Prairie, MN, 1992.
46 A. Corrigan, *J. Electrochem. Soc.*, 1987, **134**, 377–384.
47 M. Taibi, S. Ammar, N. Jouini, F. Fievet, P. Molinie and M. Drillon, *J. Mater. Chem.*, 2002, **12**, 3238–3244.
48 S. Yang, X. Wu, C. Chen, H. Dong, W. Hu and X. Wang, *Chem. Commun.*, 2012, **48**, 2773–2775.
49 J. W. Lee, J. M. Ko and J.-D. Kim, *J. Phys. Chem. C*, 2011, **115**, 19445–19454.

